encit 2020

ABCM Associação Brasileira de Engenharia e Ciências Mecânicas

18th Brazilian Congress of Thermal Sciences and Engineering
November 16–20, 2020 (Online)

ENC-2020-0065
IMPLICIT LARGE EDDY SIMULATIONS OF CONSTRICTED AND OPEN CHANNEL TURBULENT FLOWS USING A HIGH ORDER METHOD

Eron T. V. Dauricio
Instituto Tecnológico de Aeronáutica – ITA, São José dos Campos, SP, Brazil
eron.tiago90@gmail.com

João Luiz F. Azevedo
Instituto de Aeronáutica e Espaço – IAE, São José dos Campos, SP, Brazil
joaoluiz.azevedo@gmail.com

Abstract. *While Large Eddy Simulations (LES) are receiving ever more attention as the computational power rapidly increases throughout the decades, the computational costs of such calculations are still relatively high, especially for wall-bounded, high Reynolds number flows. Implicit LES (ILES) is an approach that aims at reducing the computational cost and implementation complexity, in which the explicit modeling of the subgrid scales is dropped. Hence, the artificial dissipation of the numerical method is responsible for taking into account the dissipative nature of the small scales in the overall turbulent flow, as done by the usual functional subgrid scale models. The objective of this work is to assess the applicability of the ILES approach to turbulent wall-bounded flows when using the high order discontinuous Galerkin method. Two test cases are simulated with three different configurations in order to carry out such assessment. Mean velocity profiles, Reynolds stresses and engineering coefficients are extracted and compared with reference data. The results indicate that the current approach is capable of predicting such quantities reasonably well, and certainly within engineering accuracy.*

Keywords: *Implicit LES, Wall-Bounded Flows, Discontinuous Galerkin Method, High Order Method*

1. INTRODUCTION

During the past decades, the computational fluid dynamics (CFD) community has witnessed a tremendous amount of research and important achievements in the area, owing both to the increase in computational power – and decrease in cost per arithmetic/logic operations – and developments in algorithms and numerical methods. Despite the improvements in the field, accurate simulation of turbulent flows remains an open issue, notably for wall-bounded configurations at high Reynolds numbers.

The most common approach to simulate turbulent flows is the use of the Reynolds-averaged Navier-Stokes (RANS) equations, which are obtained when an ensemble or time averaging is applied to flow variables and governing equations. This results in a system of equations for the mean flow quantities. In this case, all the turbulence effects are represented by a new, apparent stress term called *Reynolds stress* tensor, which must be modeled in order to achieve closure of the system of equations. Since the behavior of different scales of motion of turbulent flows varies widely, with large scales being highly dependent on flow geometry and boundary conditions, it becomes quite a difficult – if not impossible – task to devise turbulence models exhibiting reasonable prediction capabilities for a wide range of flow configurations with such an approach.

In contrast to the RANS approach, a straightforward way to simulate turbulent flows is to solve for the governing equations directly, without any averaging or modeling, an approach called Direct Numerical Simulation (DNS). In this case, all time and length scales of turbulent motion are captured by the numerical solution. However, since the small scales become smaller as the Reynolds number increases, *i.e.*, $\eta_\kappa/\mathcal{L}_0 \propto Re^{-3/4}$, where $\mathcal{L}_0$ represents the large scales, proportional to a characteristic length of the flow, and η_κ the small scales (Pope, 2000), the computational cost for DNS roughly grows as $Re^{37/14}$ (Choi and Moin, 2012). Thus, it becomes prohibitively high for realistic flows and configurations and such an approach is only feasible for low Reynolds number flows in simple geometries.

A compromise between the lack of turbulent scale resolution of the RANS approach and the prohibitively high computational cost of DNS is the Large Eddy Simulation (LES) approach, where the energy-containing, large scales of turbulence are directly captured by the simulation, while the small scales are modeled. In order to do so, a spatial filtering is applied to the governing equations, resulting in a system of equations for the instantaneous, filtered flow quantities. The effects of turbulent small scales are represented by a new, apparent stress term called *subgrid scale* (SGS) stress tensor, which

must be modeled in order to achieve closure of the system. In this case, since small scales are more likely to exhibit homogeneous behavior, the approach is, in principle, more amenable to universal turbulence modeling, where a single turbulence model may be successfully applied to a wide range of flow configurations.

Despite the reduced cost when compared to the DNS approach, the computational costs of LES are still relatively high for current computational capabilities and high Reynolds number flows, especially for wall-bounded flows. Such costs roughly scale as $Re^{13/7}$ (Choi and Moin, 2012), such that ways to alleviate these costs are pursued since the early stages of LES development. One such way is to employ the *Implicit LES* (ILES) approach. In ILES, the dissipative effects of small scales onto the turbulent kinetic energy cascade are accounted for by the artificial dissipation of the chosen numerical method. Hence, explicit modeling of turbulent effects is not needed, *i.e.*, the SGS term vanishes (Boris *et al.*, 1992; Oran and Boris, 1993; Grinstein *et al.*, 2007). The advantage is that the arithmetic operation count per timestep is greatly reduced, since less equations and quantities need to be computed, while largely simplifying implementation details.

The main objective of this work is to assess the applicability of the ILES approach to turbulent wall-bounded flows, with and without pressure gradient and boundary layer separation, in moderate Reynolds number conditions. In the present case, such ILES simulations are performed using a high order method. The understanding of the characteristics and predictability of the approach in such flows is important because complex phenomena, such as separation and reattachment, are commonly seen in practical applications, especially in flows of aeronautical interest. Therefore, the long term expectation is that the present results may motivate the use of the approach to more realistic geometries and configurations, as well as help define the requirements for such use in aerospace-related applications.

2. NUMERICAL METHODOLOGY

This section provides a brief description of the numerical methodology employed in the present computations.

2.1 Governing Equations

The equations to be solved by the high order numerical method are the Navier-Stokes equations for compressible flows, which may be given as

$$\frac{\partial \rho}{\partial t} + \frac{\partial \left(\rho u_i\right)}{\partial x_i} = 0 \tag{1a}$$

$$\frac{\partial \left(\rho u_j\right)}{\partial t} + \frac{\partial \left(\rho u_i u_j\right)}{\partial x_i} = -\frac{\partial p}{\partial x_j} + \frac{\partial \tau_{ij}}{\partial x_i} \tag{1b}$$

$$\frac{\partial \left(\rho E\right)}{\partial t} + \frac{\partial \left(\rho E u_i\right)}{\partial x_i} = -\frac{\partial \left(p u_i\right)}{\partial x_i} + \frac{\partial \left(u_j \tau_{ij}\right)}{\partial x_i} - \frac{\partial q_i}{\partial x_i} \tag{1c}$$

where ρ, ρu_i and ρE are the density, the three components of linear momentum and the total energy per unit volume, respectively. The latter is given by

$$\rho E = \rho e + \frac{1}{2}\rho u_i u_i \tag{2}$$

where e is the internal energy per unit mass. Moreover, τ_{ij} is the viscous stress tensor, given by

$$\tau_{ij} = \mu\left(\frac{\partial u_i}{\partial x_j} + \frac{\partial u_j}{\partial x_i}\right) + \lambda\left(\frac{\partial u_k}{\partial x_k}\right)\delta_{ij} = \tau_{ji} \tag{3}$$

Here, μ and λ are the dynamic and second viscosity coefficients, related by Stokes' hypothesis, and δ_{ij} is the Kronecker delta. Finally, q_i is the heat flux vector, given by Fourier's law of heat conduction. In the above equations, Einstein's index notation has been assumed, in which repeated indices imply summation.

2.2 Numerical Method

The numerical method employed in the present work is the high order, nodal, discontinuous Galerkin (DG) method. First, the physical domain, Ω, is split into K non-overlapping elements, Ω_k, such that

$$\Omega \approx \bigcup_{k=1}^{K} \Omega_k, \quad \bigcap_{k=1}^{K} \Omega_k = \emptyset$$

where the approximation stems from the fact that the physical boundary might not be exactly represented by the computational mesh.

The elements are then mapped from physical to standard, or computational, regions, with a mapping of the form $\Psi\colon X \to I$, where X are the physical coordinates domain and I the computational one. All computations are then carried within the computational domain.

In the nodal discontinuous Galerkin formulation, the solution is approximated by a polynomial of order N, obtained by interpolation through $N_p = N + 1$ points, or nodes. This approximate solution may be discontinuous across element interfaces, and is given, within each element, by

$$u_h^k(\boldsymbol{\xi}, t) = \sum_{p,q,r=1}^{N_p} u_h^k(\boldsymbol{\xi}_{pqr}, t)\phi_{pqr}(\boldsymbol{\xi}) \tag{4}$$

where $u_h^k(\boldsymbol{\xi}_{pqr}, t)$ are the discrete solutions at the interpolation nodes defined by coordinates $\boldsymbol{\xi}_{pqr} = (\xi_p, \eta_q, \zeta_r)$ in the computational domain, at time t, and $\phi_{pqr}(\boldsymbol{\xi})$ are the nodal basis functions, defining the solution polynomial space, $\mathcal{P} = \text{span}\{\phi_{pqr}(\boldsymbol{\xi})\}_{p,q,r=1}^{N_p}$. In this work, since the mesh is comprised of hexahedral elements only, the basis functions are obtained by a tensor product of one-dimensional Lagrange polynomials in each direction, that is,

$$\phi_{pqr}(\boldsymbol{\xi}) = \ell_p(\xi)\ell_q(\eta)\ell_r(\zeta), \qquad \ell_p(\xi) = \prod_{\substack{i=0 \\ i\neq p}}^{N_p} \frac{\xi - \xi_i}{\xi_p - \xi_i}, \tag{5}$$

where ℓ_p represents the Lagrangian interpolation polynomial for the ξ direction, and the definitions for ℓ_q and ℓ_r are similar.

The semidiscrete equations of the discontinuous Galerkin scheme are obtained by requiring that the residual of the numerical solution, within each element Ω_k, be orthogonal to a test function, v. After applying integration by parts twice and using Gauss' theorem, this requirement is expressed as

$$\int_{\Omega_k} v\frac{\partial \boldsymbol{Q}_h^k}{\partial t}\, d\boldsymbol{x} + \int_{\Omega_k} v\nabla\cdot \boldsymbol{F}_h^k(\boldsymbol{Q}_h^k, \nabla\boldsymbol{Q}_h^k)\, d\boldsymbol{x} = \int_{\partial\Omega_k} v\left(\boldsymbol{F}_h^k(\boldsymbol{Q}_h^k, \nabla\boldsymbol{Q}_h^k) - \boldsymbol{F}_h^\star\right)\cdot\hat{\boldsymbol{n}}\, d\boldsymbol{x} \tag{6}$$

where $\boldsymbol{Q}_h^k$ is the discrete vector of conserved variables, and $\boldsymbol{F}_h^k = [f, g, h]^T$ the discrete flux vector, the definition given by Eqs. (1), and approximated as in Eq. (4). The space of test functions, v, is the same as the space of solution polynomials, $\mathcal{P}$, defined above. After substitution of the test function, v, and the approximate solution as in Eq. (4), the semidiscrete equations are obtained, for each element Ω_k, and may be given as

$$\boldsymbol{\mathcal{M}}^k\frac{d\mathbf{Q}_h^k}{dt} + \boldsymbol{\mathcal{T}}^k\cdot\boldsymbol{F}_h^k = \sum_{e\in\partial\Omega^k}\int_{\partial\Omega^k}\ell_i(\mathbf{x})\left[\boldsymbol{F}_h^k - \boldsymbol{F}_h^\star\right]\cdot\hat{\boldsymbol{n}}\, d\mathbf{x} \tag{7}$$

where $\boldsymbol{\mathcal{M}}^k$ is the element mass matrix, and $\boldsymbol{\mathcal{T}} = \left[\mathcal{S}_x^k, \mathcal{S}_y^k, \mathcal{S}_z^k\right]$ the vector of stiffness matrices. It should be noted that a transformation from physical to computational domain must be made, as stated before, and hence transformation metric terms will appear on the semidiscrete equations above. A complete description, including such transformations and the metrics used, is detailed in Hindenlang *et al.* (2012).

In Eqs. (6) and (7), $\boldsymbol{F}_h^\star$ is a *numerical flux*, introduced so that a common value for the fluxes may be obtained at element interfaces. For the inviscid part of the fluxes, it is calculated by solving a Riemann problem at the interface, whereas for the viscous fluxes it is given by simple averaging between the fluxes on both sides of the interface. In this work, Roe's approximate Riemann solver with an entropy correction is used (Toro, 2009). In addition, since weak variational formulations using discontinuous function spaces – such as the discontinuous Galerkin scheme – are not suitable for directly discretizing higher order derivative operators, the lifting scheme of Bassi and Rebay (2000) is used in order to discretize the second order derivatives appearing after evaluation of the divergence of the viscous fluxes.

For stabilization of the numerical solution, a skew-symmetric, split formulation of the inviscid fluxes is employed, using the Pirozzoli (2011) split form, which, for the x-component of the inviscid flux vector, may be given as

$$f_I^\# = \begin{bmatrix} \{\!\{\rho\}\!\}\{\!\{u\}\!\} \\ \{\!\{\rho\}\!\}\{\!\{u\}\!\}^2 + \{\!\{p\}\!\} \\ \{\!\{\rho\}\!\}\{\!\{v\}\!\}\{\!\{u\}\!\} \\ \{\!\{\rho\}\!\}\{\!\{w\}\!\}\{\!\{u\}\!\} \\ \{\!\{\rho\}\!\}\{\!\{H\}\!\}\{\!\{u\}\!\} \end{bmatrix}, \quad \text{with} \quad \{\!\{a\}\!\}_{im} = \frac{1}{2}\left(a_i + a_m\right). \tag{8}$$

where the subscript I indicates the *inviscid* part of the flux. Similar expressions are obtained for the flux components in the y and z direction. This form of the flux is kinetic-energy preserving (Jameson, 2008).

The implementation of such split form relies on a summation-by-parts property of the discrete derivative matrix, $\boldsymbol{\mathcal{D}} = \left(\boldsymbol{\mathcal{M}}^k\right)^{-1} \boldsymbol{\mathcal{S}}_i^k$, when written for the nodal discontinuous Galerkin scheme using Gauss-Lobatto-Legendre points as interpolation nodes. In this case, the discrete derivative of the volumetric inviscid flux term in Eq. (7) may be approximated as

$$\boldsymbol{\mathcal{D}} \boldsymbol{f}_I \approx 2 \sum_{m=1}^{N_p} \mathcal{D}_{im} f_I^{\#,l}(Q_{ijk}^l, Q_{mjk}^l)$$

and similarly for the flux components in the y and z direction. In the above equation, the superscript l represents a component of the inviscid flux f_I and the corresponding component of the conserved variables vector. In order to obtain a globally kinetic-energy preserving scheme, the numerical interface, Riemann fluxes are modified accordingly, using this same split formulation. An extensive description of such approach and its implementation may be found in Gassner *et al.* (2016).

In the current work, the *implicit LES* (ILES) approach is employed in the simulations. In this approach, there is no subgrid scale turbulence models added to the system of equations in Eq. (1), and the numerical dissipation is responsible for the effects of the small scales of turbulence onto the larger ones. In a DG context, the numerical dissipation depends mainly on the interface Riemann fluxes employed and the approximation to the gradient of conserved variables, obtained by the lifting scheme for the second order derivative terms in the viscous fluxes (Moura *et al.*, 2017).

The semidiscrete equations are advanced in time using the fourth-order, five-stage, low-storage explicit Runge-Kutta scheme of Carpenter and Kennedy (1994). The effective implementation of the aforementioned numerical method is accomplished with the Flexi computational software (Hindenlang *et al.*, 2012; Krais *et al.*, 2019), through which high-efficiency, parallel computations are achieved.

2.3 Computational Geometries and Configurations

This work is concerned with applying the ILES approach to two different geometries. The first one is an open channel, with periodic boundary conditions in the span- and stream-wise directions, and wall boundary conditions in the bottom and top planes of the channel. The second geometry is a channel with constrictions in both ends, where periodic boundary conditions in the stream-wise direction render a flow in a wavy channel, usually called the periodic hill test case. In the span-wise direction, periodic boundary conditions are also employed for the periodic hill, while both bottom and top boundaries are considered as walls. Figure 1 presents outlines of both geometries.

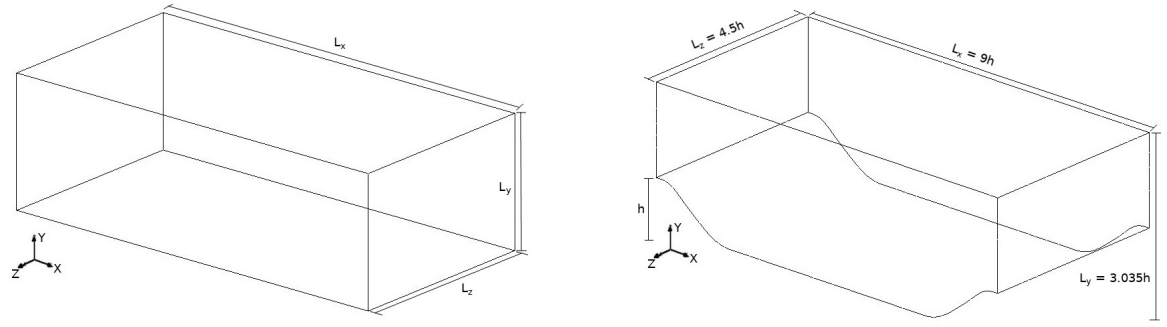

(a) Channel flow. Dimensions are $L_x = 2\pi\delta$, $L_y = 2\delta$, $L_z = \pi\delta$, with the half-channel width $\delta = 1$.

(b) Periodic hill flow. Hill crest height, $h = 1$.

Figure 1. Outline of the computational geometries for which the flows are simulated.

For the channel flow, two simulations are performed with Reynolds numbers of $Re_\tau = 590$ and $Re_\tau = 950$, based on viscous units. Mean flow and Reynolds stress quantities are evaluated and discussed. The references to which the present results are compared to are the DNS simulations of Moser *et al.* (1999) and Del Álamo *et al.* (2004), for the cases of Re_τ equal to 590 and 950, respectively.

For the periodic hill test case, the simulation is performed for a Reynolds number of $Re = 10,595$, based on the hill height and the bulk velocity above the crest. The results are to be compared to the data of Fröhlich *et al.* (2005) and Temmerman *et al.* (2003), both of which are LES simulations. While the former is a highly resolved LES and will, therefore, be considered as the benchmark result, the latter contains both highly resolved and underresolved LES simulations, the results of which are relevant in guiding the conclusions for the simulations in the present work.

3. RESULTS AND DISCUSSION

3.1 Plane Channel Flow

3.1.1 Mesh Characteristics

Two different meshes are used for each Reynolds number flow, and their mesh spacing characteristics, based on viscous units and an equidistant interpolation node distribution within an element, are shown in Table 1.

Table 1. Plane channel flow mesh characteristics for each Reynolds number.

Re_τ	Δx^+	Δz^+	Δy^+_{min}	Δy^+_{max}	$\Delta y_{max}/\delta$
590	29	14.5	1.3	8	0.013
950	50	24.9	0.7	24.2	0.025

The Δy^+_{min} is related to the first node adjacent to the wall, whereas Δy^+_{max} and $\Delta y_{max}/\delta$ are related to the first node adjacent to the channel centerline. A reasonable, recommended mesh – although not excessively fine – should have $(\Delta x^+, \Delta z^+) \approxeq (40, 20)$, while in the y direction, it should range from $\Delta y^+ \approxeq 1$ near the wall to $\Delta y/\delta \approxeq 0.02$ near the end of the outer layer, and $\Delta y/\delta \approxeq 0.05$ at the edge of the boundary layer (Larsson *et al.*, 2016). In addition, the y-direction spacing should vary linearly.

Both simulations are run up to 20 eddy turnover time (ETT), given by $ETT = tu_\tau/\delta$, and a polynomial order of $N = 4$, resulting in a fifth order method.

3.1.2 Test Case for $Re_\tau = 590$

Results obtained for the case of $Re_\tau = 590$ are shown in Fig. 2, where the mean velocity profile, in viscous units, and the Reynolds stresses normalized by the friction velocity, $u_\tau = \sqrt{\tau_w/\rho}$, are plotted. The reference data is the DNS simulation of Moser *et al.* (1999) at the same Reynolds number.

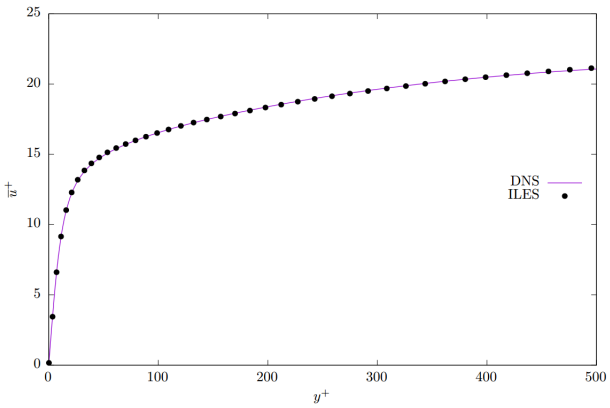

(a) Mean velocity profile in viscous units

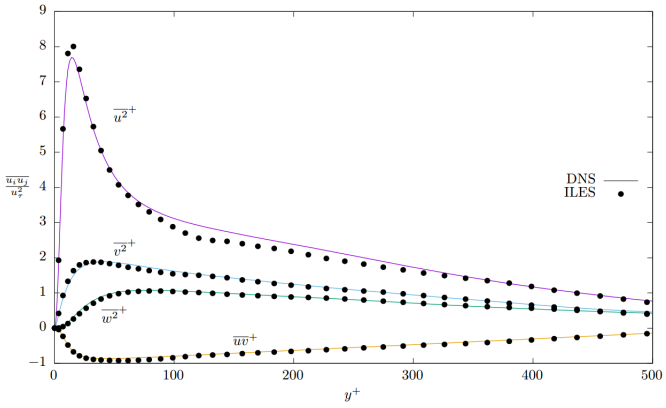

(b) Second moment of Reynolds stresses normalized by friction velocity

Figure 2. Mean velocity profile and second moment of Reynolds stresses at $Re_\tau = 590$. ILES represents the present calculations whereas DNS refers to the results of Moser *et al.* (1999).

An excellent agreement is observed for the mean velocity profile and normal Reynolds stresses in the y and z direction, across the full range of the channel half-width, whereas some discrepancy may be seem for the normal Reynolds stress in the x direction. The results for the shear component of the Reynolds stress tensor, $\overline{uv}^+$, are also very good. For this Reynolds number, the log-layer comprises the region $30 \lesssim y^+ \lesssim 180$. Since this is a low Reynolds number flow, the overlap layer between the inner, viscous region and the outer layer is very small. This means that, for $y^+ \gtrsim 50$, viscous effects on the velocity profile are negligible.

As can be seen, the discrepancy observed for the normal Reynolds stress in the x direction is within the outer layer. In this region, the production, $\mathcal{P}$, and dissipation of turbulent kinetic energy, ε, roughly balances each other, *i.e.* $\mathcal{P}/\varepsilon \approx 1$ (Pope, 2000). Since the Reynolds stresses are underestimated in this region, it seems that the ILES simulation is either not able to correctly capture turbulence production mechanisms, or there is an excessive dissipation. Because the mesh characteristics for this case are well within the recommended ranges for a reasonably fine LES mesh, this hints at the possibility of an excess of dissipation coming from the numerical method – usually through the numerical, Riemann interface flux. Tests are being performed at the present time in order to attempt to further understand such behavior. For

the region $y^+ > 300$, where production of turbulent kinetic energy starts to fall and the dissipation dominates, the ILES predictions are again in excellent agreement with the DNS data.

3.1.3 Test Case for $Re_\tau = 950$

The results for the simulation at $Re_\tau = 950$ are shown in Fig. 3. The reference DNS data are that of Del Álamo *et al.* (2004). It is clear that the results are in poorer agreement in comparison to the results of the previous section, for $Re_\tau = 590$.

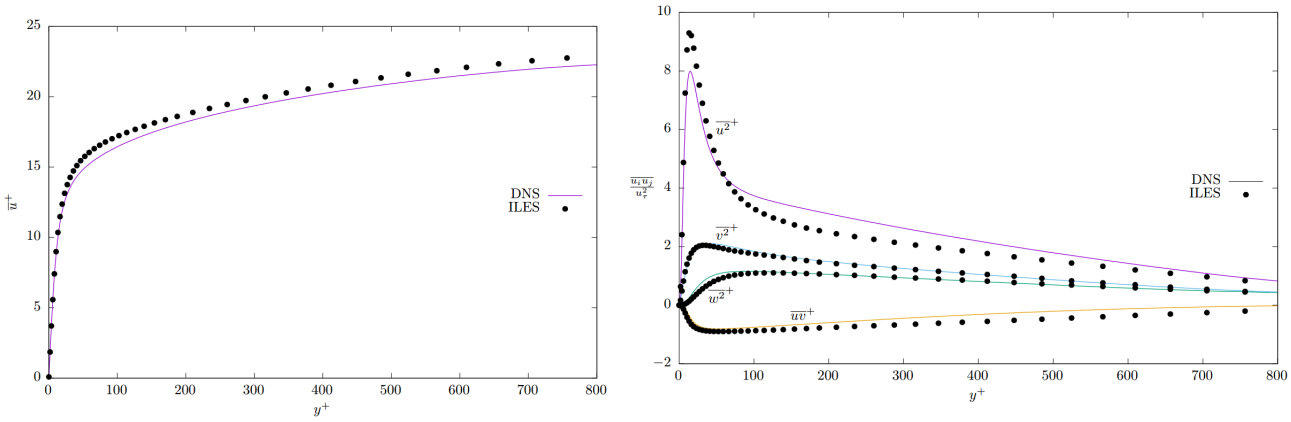

(a) Mean velocity profile in viscous units

(b) Second moment of Reynolds stresses normalized by friction velocity

Figure 3. Mean velocity profile and second moment of Reynolds stresses at $Re_\tau = 950$. ILES represents the present calculations whereas DNS refers to the results of Del Álamo *et al.* (2004).

The mean velocity profile for this case only matches the DNS reference data at the viscous wall region, $y^+ \lesssim 50$, being overpredicted across the whole log and outer layers, up to the channel half-width. For this flow, the log-layer comprises the region $30 \lesssim y^+ \lesssim 280$, whereas the overlap between the inner and outer region now becomes more significant, roughly given by the interval $50 \lesssim y^+ \lesssim 100$. In practice this means that the dynamics of the wall, reflected on the flow variables u_τ and y^+, have important contributions further away from the wall.

Apart from the clear mismatch on the prediction of the mean velocity profile above the viscous wall region, the Reynolds stresses are well predicted throughout the whole channel half-width, except for the $\overline{u^2}^+$ component. The simulation could correctly capture the location of the peak on the normal Reynolds stress in the x direction, though its value is highly overestimated. In the overlap region, at $y^+ \approx 70$, the behavior of the prediction shifts, and this component is then underestimated. This misprediction is reflected up to $y^+ \approx 700$, near the channel centerline. The underprediction of the fluctuation in the x direction is also reflected on the results for the $\overline{uv}^+$ component of the Reynolds stress, which has a lower value throughout the channel half-width, compared to the reference DNS data. On the other hand, the results for the normal Reynolds stress components on the y and z directions agree well with the DNS data, except for the overlap region, where they are only slightly underestimated.

From the mesh characteristics shown in Table 1, the mesh spacing on the y direction is well within the recommended range. However, those for the x and z directions are slightly above the recommended value, and the lack of resolution in these directions may be the cause of the poor results exhibited by the statistical data in the x and z directions, primarily. Another trend observed by inspecting Figures 2 and 3 is that the higher the Reynolds number, the higher the peak predicted for the normal Reynolds stress in the x direction. This is a direct consequence of a greater production-to-dissipation ratio, $\mathcal{P}/\varepsilon$, in this region.

Hence, it seems that the numerical dissipation is high from the outer layer to the edge of the boundary layer, but low within the inner layer, such that the rate between production and dissipation is unbalanced in both regions, and the higher the Reynolds number, the higher this unbalancing. Finally, mean velocity profiles and reference DNS data for both cases are plotted in Fig. 4 in semi-log scale. From this figure, the overprediction of the ILES simulation in the case of $Re_\tau = 950$, especially within the log region, becomes clearer.

3.2 Periodic Hill Flow

For the periodic hill case, a single mesh is used, again moderately fine, but coarser than those used for the channel flows. The polynomial order of the numerical approximation is $N = 3$ for this simulation, resulting in a fourth order method. The Reynolds number of the simulation is $Re = 10,595$, based on the hill height and the bulk velocity above the

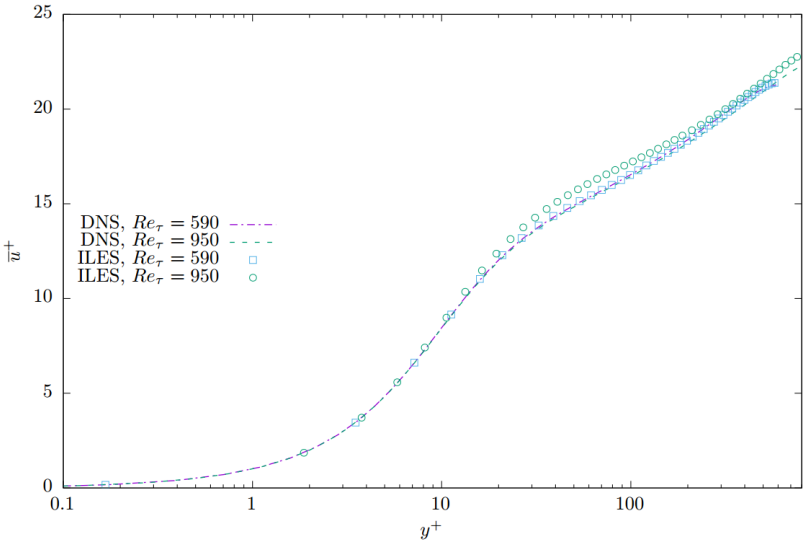

Figure 4. Mean velocity profiles, normalized by friction velocity, and in semi-log scale, for both Reynolds number cases and the respective DNS reference data.

hill crest, that is,

$$Re = \frac{U_b h}{\nu},$$

with

$$U_b = \frac{1}{(L_y - h)} \int_h^{L_y} \overline{u}(y)\, dy,$$

taken at the inflow plane. This Reynolds number matches that of the highly resolved LES simulations in references Fröhlich *et al.* (2005) and Temmerman *et al.* (2003), both of which are used in the comparisons to follow. The latter also contains moderately resolved LES simulations, which aid comparisons and discussions of the present results. To the authors' knowledge, there is no DNS simulations of this case.

The current test case is a fairly complicated flow, exhibiting adverse pressure gradient which is strong enough to cause the boundary layer to separate. After separation, a recirculating flow region is formed, followed by boundary layer reattachment just before a region of favorable pressure gradient. Mean flow quantities extracted for the present analysis refer to those of a longitudinal slice of the geometry after averaging all computational planes in the z direction.

Mesh spacing at the first node adjacent to the lower wall are shown in Fig. 5, in viscous units. In this figure, horizontal dashed lines indicate the recommended values for each direction, as discussed earlier. For comparison, mesh spacing in the y direction for the medium grid used in Temmerman *et al.* (2003) is also shown. The variations in the viscous mesh spacings are due to the wall shear stress variations along the channel length, as opposed to a constant wall shear stress in the case of plane channel flow, leading to variable friction velocity, $u_\tau = \sqrt{\tau_w/\rho}$, and, hence, variable viscous characteristic length, $\delta_v = \nu/u_\tau$.

It can be seen that the mesh spacing in the x direction is within the recommended value of $\Delta x^+ \approx 40$ throughout the channel length, except for the region of favorable pressure gradient, where the wall shear stress strongly increases, leading to higher friction velocity, u_τ, and, consequently, lower viscous characteristic length, δ_v, such that the ratio $\Delta x/\delta_v = \Delta x^+$ increases. For the z direction, the mesh spacing is only within the recommended value of $\Delta z^+ \approxeq 20$ in the region of adverse pressure gradient, that is, x/h up to approximately 2. Then, the viscous mesh spacing in this direction becomes roughly 30 for the rest of the channel length, again with the exception of the region of favorable pressure gradient. For the y direction, the mesh spacing is approximately unit only within a tiny region down the hill, $0.7 \lesssim x/h \lesssim 1.3$. For the rest of the channel, it is about 5, taking values up to 10 in the region of favorable pressure gradient. Lastly, the mesh spacing in the y direction for the present simulation compares well with the medium grid of Temmerman *et al.* (2003), both qualitatively and quantitatively.

One aspect to notice is that, in order to speed up the simulations and save computational resources, the mesh is much coarser in the y direction near the upper wall. The main concern in this work is to assess the capability of the ILES approach using a high order DG method for simulations exhibiting adverse pressure gradient and boundary layer separation. Since the flow in the upper wall have limited influence on the flow near the bottom wall (Temmerman *et al.*, 2003), this mesh coarsening may be done with no losses to the present analysis and results.

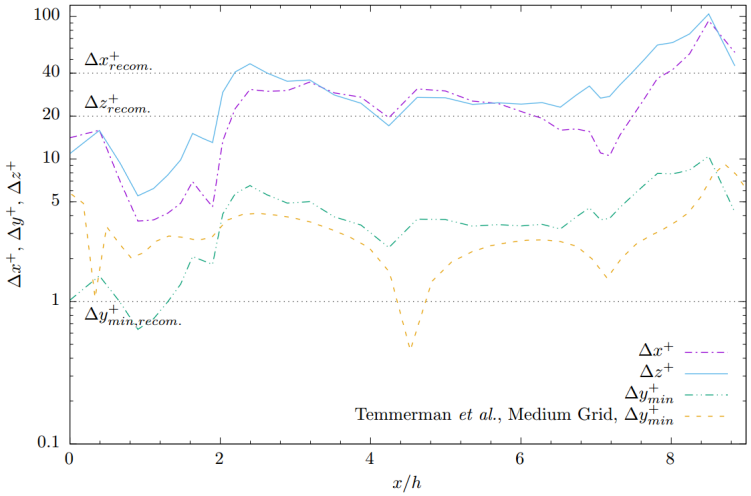

Figure 5. Mesh spacings, in viscous units, for the periodic hill simulation in all three directions at the first node adjacent to the lower wall. Horizontal dashed lines indicate the recommended values for each direction. Mesh spacing in the y direction for the medium grid used in Temmerman *et al.* (2003) is also plotted for comparison.

Skin friction coefficient distribution obtained for this simulation is presented in Fig. 6, where it is compared with that obtained in the highly resolved LES simulation of Fröhlich *et al.* (2005). Both the separation and reattachment points are correctly captured when compared to this reference. The overall behavior of the skin friction coefficient is also correctly represented by the present simulation, although the distribution obtained in the present calculation is slightly more oscillatory than the reference data.

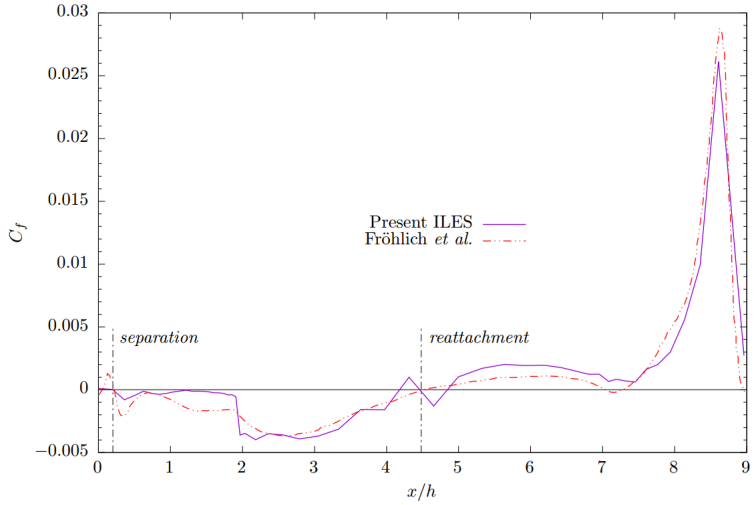

Figure 6. Skin friction coefficient distribution for the present simulation, compared to the reference Fröhlich *et al.* (2005). Vertical dashed lines show the points of boundary layer separation and reattachment.

According to the predicted skin friction coefficient, there is a small, second region of recirculating flow just after the reattachment of the boundary layer following the main separation bubble. This behavior cannot be seen in any of the reference simulations (Fröhlich *et al.*, 2005; Temmerman *et al.*, 2003). On the other hand, the highly resolved simulation of Fröhlich *et al.* (2005) also exhibits another point where the boundary layer separates, just before the region of favorable pressure gradient, $x/h \approx 7$. However, in this case the region is so small and the skin friction is so close to zero that a separation bubble is absent.

Figure 7 shows a longitudinal slice of the periodic hill where mean velocity profiles, normalized by the bulk velocity, U_b, are obtained for the present simulation after averaging in the z direction, at two different streamwise sections. For comparison, mean velocity profiles obtained in the highly resolved LES simulations of Temmerman *et al.* (2003) and Fröhlich *et al.* (2005) are also shown. The mean velocity profiles obtained for the present simulation agree very well with both high resolution references at both sections, *i.e.* $x/h = 2$ and $x/h = 6$. The first section is well within the recirculating bubble, as can be seen from Fig. 6 and the negative mean velocity near the bottom wall, whereas the second section shows the recovering of the boundary layer after reattachment. These velocity profiles are a clear indication that

the present ILES approach using a high order DG scheme is able to capture mean velocity profiles even in the presence of adverse pressure gradient, boundary layer separation and reattachment, and recirculating regions.

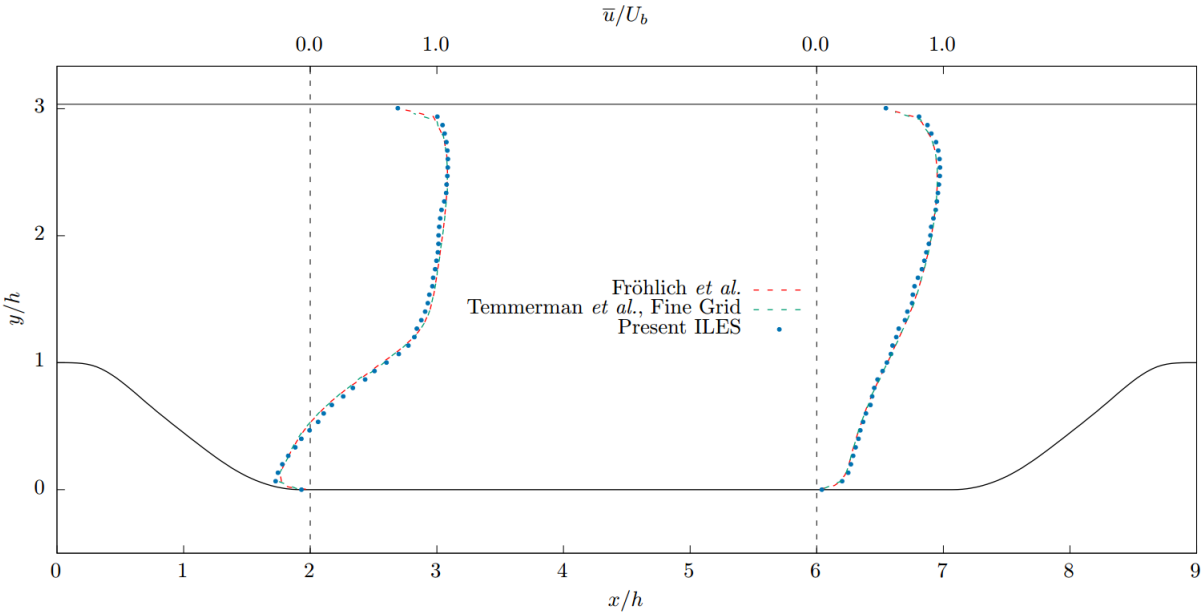

Figure 7. Longitudinal slice of the periodic hill, showing the mean velocity profiles at two different streamwise sections. Data are from the present simulation and both highly resolved LES simulations of Temmerman *et al.* (2003) and Fröhlich *et al.* (2005).

A more detailed comparison can be made by inspecting Fig. 8, where the mean velocity profiles for the present simulation and both medium and fine grid simulations of Temmerman *et al.* (2003) are shown, at the same two streamwise sections. The first aspect to notice is that, from $y/h \approxeq 1.5$ upwards, the velocity profiles for the present simulation exhibits some oscillations. This is caused by a coarser mesh near the upper wall, as stated above, influencing the solution up to this point. In addition, the fact that the velocity profiles are well behaved below $y/h \approxeq 1.5$ is also an indication that the solution near the bottom wall is not influenced by the mesh coarseness of the upper wall. More importantly, though, is

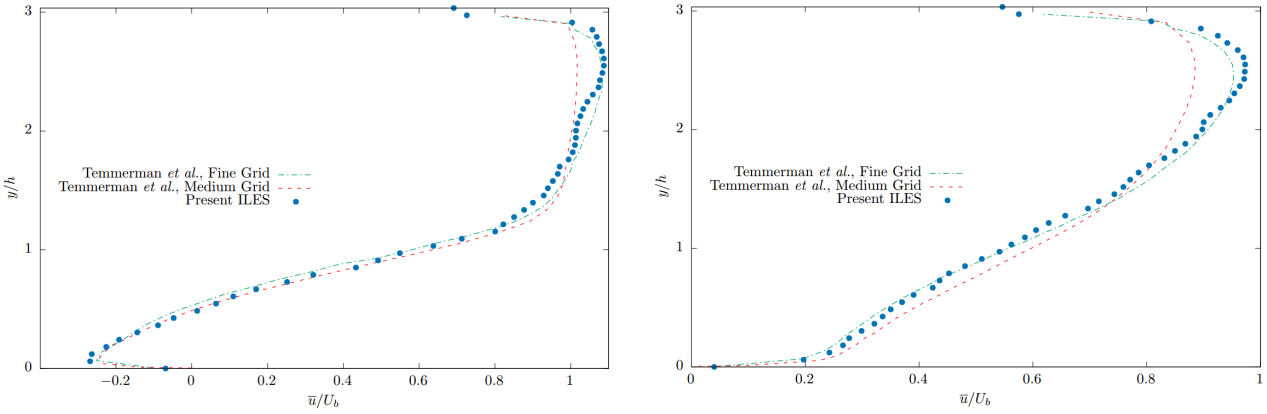

(a) $x/h = 2$ (b) $x/h = 6$

Figure 8. Mean velocity profiles at two different streamwise sections. Data are from the present simulation and the fine and medium resolution LES simulations of Temmerman *et al.* (2003).

the fact that the present simulation follows the highly resolved, fine grid solution much more closely than the medium grid solution in the reference data. This is true even for the velocity profile near the upper wall, where the resolution of the present simulation is not even close to the recommended resolution for a well resolved LES simulation. Hence, these results demonstrate, once again, that the ILES approach using a high order DG method is very well suited for fairly complex simulations, even under moderately low resolution meshes.

The exact cause of such good results, however, cannot be determined solely based on the data shown. These results might be due to a better behavior of small scale dissipation implicitly added by the numerical dissipation, or even the method's higher order, leading to a dissipation that is steeper and more concentrated on the small scale region of the

energy cascade. Further results and a more complete set of simulations are needed in order to systematically point out the reasons of the method success – even though it is clear that the approach used in the present work provides excellent results, at least for mean velocity profiles, Reynolds stresses and engineering coefficients. Overall, the results presented in this work support and strengthen the feasibility and applicability of the ILES approach in conjunction with a high order DG method for simple and fairly complex flows, under moderate Reynolds numbers.

4. CONCLUSIONS

In the present work, the feasibility and applicability of the implicit LES approach with a high order DG method has been assessed. In order to do so, two test cases are simulated, with three different configurations. The plane channel turbulent flow case is simulated for Reynolds numbers of $Re_\tau = 590$ and 950, whereas the periodic hill case is simulated for a Reynolds number of $Re = 10\,595$, based on the hill height and bulk velocity above the hill crest.

For the simple, plane turbulent channel flows, the results indicate that the current high order method is capable of predicting the mean velocity profiles and Reynolds stresses reasonably well. The predictions deteriorate as the Reynolds number increases. The cause of the mispredictions observed may be due to an insufficient numerical dissipation near the wall, where production greatly dominates dissipation, and, on the other hand, an excessive dissipation for the outer layer up to the boundary layer edge. Since this numerical dissipation is implicitly added by the numerical method, it is not possible to explicitly adjust it in order to further investigate this claim. One way to assess the dissipative characteristics of the numerical method on the overall flow is to change the interface Riemann fluxes, and also run new simulations with different orders of accuracy. The fact that the current channel flow simulations are run using a fifth order scheme may also be the reason for this unbalancing of turbulent production-to-dissipation ratio. By increasing the order of accuracy, turbulent production mechanisms tend to be captured more accurately, while dissipation tends to decrease.

In the case of the periodic hill flow, the primary goal is to assess the capability of the current approach to correctly capture the separation and reattachment points. Results for the skin friction coefficient clearly indicate that the current approach is able to correctly capture such boundary layer features, even under a moderately coarse mesh. In addition, mean velocity profiles at two distinct streamwise sections are compared, and the present results agree very well with the reference data, which indicates that the ILES approach using a high order DG scheme is also capable of correctly predicting mean flow quantities, such as velocity profiles. In this case, the mismatch between the current results and the reference data are clearly associated to a mesh coarseness near the upper wall, rather than associated to the numerical method itself.

Even though both mesh resolution and order of accuracy may play a non-negligible role on the solution, overall, the results presented in this work support and strengthen the feasibility and applicability of the ILES approach in conjunction with a high order DG method for simple and fairly complex flows, under moderate Reynolds numbers.

5. ACKNOWLEDGEMENTS

The authors would like to acknowledge the financial support for the present research in the form of a doctoral scholarship from the São Paulo Research Foundation (FAPESP), under the Grant No. 2018/05524-1. The authors wish to also acknowledge the computational resources provided by the Center for Mathematical Sciences Applied to Industry (CeMEAI), a Center of Research, Innovation and Diffusion (CEPID), funded by FAPESP under the Research Grant No. 2013/07375-0. Partial support for the present work is also provided by Conselho Nacional de Desenvolvimento Científico e Tecnológico, CNPq, under the Research Grant No. 309985/2013-7.

6. REFERENCES

Bassi, F. and Rebay, S., 2000. "A high-order discontinuous Galerkin method for compressible turbulent flows". In B. Cockburn, G.E. Karniadakis and C.W. Shu, eds., *Discontinuous Galerkin Methods: Theory, Computation and Applications*, Springer-Verlag, Lecture Notes in Computational Science and Engineering.

Boris, J.P., Grinstein, F.F., Oran, E.S. and Kolbe, R.L., 1992. "New insights into large eddy simulation". *Fluid Dynamics Research*, Vol. 10, No. 4–6, pp. 199–228.

Carpenter, M.H. and Kennedy, C.A., 1994. "Fourth-order 2N-storage Runge-Kutta schemes". NASA-TM-109112, NASA Langley Research Center.

Choi, H. and Moin, P., 2012. "Grid-point requirements for large eddy simulation: Chapman's estimates revisited". *Physics of Fluids*, Vol. 24, No. 1, pp. 011702.1–011702.5.

Del Álamo, J.C., Jiménez, J., Zandonade, P. and Moser, R.D., 2004. "Scaling of the energy spectra of turbulent channels". *Journal of Fluid Mechanics*, Vol. 500, pp. 135–144.

Fröhlich, J., Mellen, C.P., Rodi, W., Temmerman, L. and Leschziner, M.A., 2005. "Highly resolved large-eddy simulation of separated flow in a channel with streamwise periodic constrictions". *Journal of Fluid Mechanics*, Vol. 526, pp. 19–66.

Gassner, G.J., Winters, A.R. and Kopriva, D.A., 2016. "Split form nodal discontinuous Galerkin schemes with summation-by-parts property for the compressible Euler equations". *Journal of Computational Physics*, Vol. 327, pp. 39–66.

Grinstein, F.F., Margolin, L.G. and Rider, W.J., 2007. *Implicit Large Eddy Simulation: Computing Turbulent Fluid Dynamics*. Cambridge University Press.

Hindenlang, F., Gassner, G.J., Altmann, C., Beck, A., Staudenmaier, M. and Munz, C.D., 2012. "Explicit discontinuous Galerkin methods for unsteady problems". *Computers and Fluids*, Vol. 61, pp. 86–93.

Jameson, A., 2008. "Formulation of kinetic energy preserving conservative schemes for gas dynamics and direct numerical simulation of one-dimensional viscous compressible flow in a shock tube using entropy and kinetic energy preserving schemes". *Journal of Scientific Computing*, Vol. 34, No. 2, pp. 188–208.

Krais, N., Beck, A., Bolemann, T., Frank, H., Flad, D., Gassner, G., Hindenlang, F., Hoffmann, M., Kuhn, T., Sonntag, M. and Munz, C.D., 2019. "FLEXI: A high order discontinuous Galerkin framework for hyperbolic-parabolic conservation laws".

Larsson, J., Kawai, S., Bodart, J. and Bermejo-Moreno, J., 2016. "Large eddy simulation with modeled wall-stress: Recent progress and future directions". *Mechanical Engineering Reviews*, Bulletin of the JSME, Vol. 3, No. 1, pp. 15–00418.

Moser, R.D., Kim, J. and Mansour, N.N., 1999. "Direct numerical simulation of turbulent channel flow up to $Re_\tau = 590$". *Physics of Fluids*, Vol. 11, No. 4, pp. 943–945.

Moura, R.C., Mengaldo, G., Peiró, J. and Sherwin, S., 2017. "An LES setting for DG-based implicit LES with insights on dissipation and robustness". In M.L. Bittencourt, N.A. Dumont and J.S. Hesthaven, eds., *Spectral and High Order Methods for Partial Differential Equations ICOSAHOM 2016*, Springer-Verlag, Vol. 119 of *Lecture Notes in Computational Science and Engineering*, pp. 161–173.

Oran, E.S. and Boris, J.P., 1993. "Computing turbulent shear flows – A convenient conspiracy". *Computers in Physics*, Vol. 7, No. 5, pp. 523–533.

Pirozzoli, S., 2011. "Numerical methods for high-speed flows". *Annual Review of Fluid Mechanics*, Vol. 43, pp. 163–194.

Pope, S.B., 2000. *Turbulent Flows*. Cambridge University Press. 771 p.

Temmerman, L., Leschziner, M.A., Mellen, C.P. and Frölich, J., 2003. "Investigation of wall-function approximations and subgrid-scale models in large eddy simulation of separated flow in a channel with streamwise periodic constrictions". *International Journal of Heat and Fluid Flow*, Vol. 24, No. 2, pp. 157–180.

Toro, E.F., 2009. *Riemann Solvers and Numerical Methods for Fluid Dynamics*. Springer-Verlag, 3rd edition.

7. RESPONSIBILITY NOTICE

The authors are solely responsible for the printed material included in this paper.